JACS
JOURNAL OF THE AMERICAN CHEMICAL SOCIETY
pubs.acs.org/JACS
Article

Structure Dependent Accessibility of Active Sites Governs Catalytic Activity and Stability of Iridium Oxides in the Acidic Oxygen Evolution Reaction

Yeonsu Kim, Jeonghyeon Kim, Sang-Il Choi,* Hangil Lee,* and Hyun S. Ahn*

Cite This: J. Am. Chem. Soc. 2026, 148, 957−966
Read Online

ABSTRACT: Deep understanding of the structural influence on the activity−stability relationship of iridium oxides in acidic oxygen evolution reaction (OER) is desired for better catalyst designs and, consequently, improved atom efficiency of the rare-earth element. However, identifying the variables governing the reaction mechanism remains a challenge in environments where multistep reactions and catalyst degradation occur simultaneously. Surface interrogation scanning electrochemical microscopy (SI-SECM) was employed to directly quantify the transient reactivity of OER intermediates on iridium oxide surfaces (amorphous IrO_x and crystalline IrO_2). Electrochemical measurements revealed a structure dependence of the electrolyte-accessible depth of active site layers, the variation of which controls the kinetics of charge storage and ultimately governs the OER catalysis. Contrary to the common models in the literature, effective charge storage exhibited little influence on the lowering of the OER kinetic barrier. Rather, the activity of iridium oxide catalysts was governed by the electrolyte permeability of the material, which controlled the number of active sites.

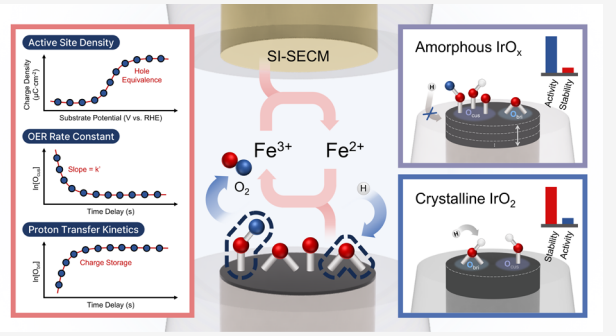

1. INTRODUCTION

Climate change induced by fossil-fuel-driven activities amplified the demand for the development of renewable energy technologies. One of the most attractive large-scale energy storage solutions is the production of green hydrogen via proton exchange membrane water electrolysis (PEMWE);[1,2] however, under highly acidic and oxidizing conditions, iridium oxide remains the sole catalyst capable of achieving a balance between activity and stability for the kinetically sluggish oxygen evolution reaction (OER) at the anode.[3,4] Unfortunately, iridium is scarce and the reported catalytic durability is limited.[5−7] Therefore, a fundamental mechanistic understanding of the acidic OER on iridium oxides is desired for the preparation of catalysts that meet the stability and activity requirements to be competitive at high current scales.

The activity and stability of a catalyst are sharply influenced by its crystal structure.[8] In the case of iridium oxides, amorphous IrO_x is documented to exhibit superior activity for OER, with a trade-off in stability, compared to that of crystalline IrO_2.[9−11] Important OER intermediates are electron-deficient oxygen species (O^{1-}, oxygen species with more electrophilic hole character), which are categorized into two sites with distinct redox behavior: (1) bridging oxygen (O_{bri}, μ_2-O) and (2) coordinatively unsaturated site oxygen (O_{cus}, μ_1-O).[12−15] Recent investigations attempted to differentiate the two species in potential space and ascertain the respective roles in catalysis; however, the exact functions of O_{bri} and O_{cus} in the OER remain unclear. Inspired by Jones and co-workers' establishment of the correlation between O^{1-} charge accumulation (i.e., increased surface hole (h^+) coverage (θ^{h+})) and OER activation energy,[16] significant research efforts were focused on elucidating the crystal structure dependence of the reactivity of the electron-deficient oxygen species.[17,18] In 2022, an *operando* X-ray spectroscopy investigation by Mom and co-workers demonstrated that the degree of deprotonation of the lattice oxygen species depended on sample crystallinity, and the deprotonated oxygen population influences the kinetics of both OER and iridium dissolution.[10] Recent work by Stephens and co-workers revealed that crystal structure dependent active site coverage regulates the balance between *O binding energy and adsorbate−adsorbate interactions, thereby controlling the reaction kinetics.[19] Despite these insightful findings, the fundamental link between the lattice structure of the catalyst and the redox behavior (both the intermediate adsorbate and the active site) remains to be further elucidated. The main challenge lies in the lack of

Received: September 23, 2025
Revised: December 4, 2025
Accepted: December 5, 2025
Published: December 29, 2025

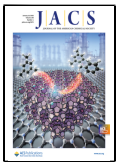

https://doi.org/10.1021/jacs.5c16721
J. Am. Chem. Soc. 2026, 148, 957−966

Scheme 1. Representation of the SI-SECM Redox Titration Sequence: (a) Resting at Open Circuit Potential (OCP), (b) Titrand (O^{1-}) Generation by Substrate Pulse, and (c) Titrand Consumption by (i) Titrant (Fe^{2+}) Generation, through (ii) OER, and (iii) Protonation during Delay Time

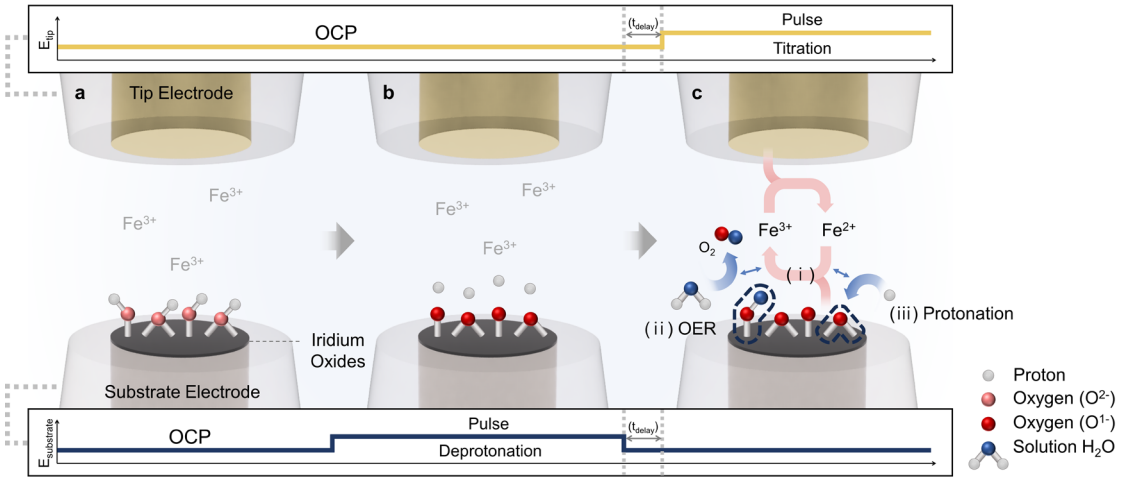

quantitative analytical means for the detection of the transient surface redox species involved in the catalytic cycle.[20,21]

In this regard, surface interrogation scanning electrochemical microscopy (SI-SECM) offers an attractive approach for catalyst surface analysis.[22−24] The SI-SECM technique enables time-resolved detection of electrolyte-accessible surface sites, independent of the underlying bulk. Notably, this titration technique has provided critical mechanistic insights into various electrochemical energy conversion reactions by accurate quantification of the transient reactivity of surface species, including active site density, intermediate kinetics, and lifetimes.[25−29]

In this work, we systemically identify the key factors influencing the activity and stability of two catalyst structures, amorphous IrO_x and crystalline IrO_2 by SI-SECM. We directly quantified the active site density and activity of electron-deficient oxygen species for each catalyst. In the process, the much-discussed charge storage mechanism of iridium oxide in the acidic OER was empirically demonstrated through time-dependent titrations. Quantitative determination of the proton transfer kinetics of the electron-deficient oxygen species revealed the link between the structure-dependent electrolyte permeability and the ease of oxidative charge accumulation. Facilitated oxidative charge accumulation exhibited little impact on lowering the activation energy of the OER, and the key factor driving the catalytic activity was the electrolyte-accessible active site density. Furthermore, the penetration of electron-deficient oxygen species (μ_2 and μ_1) into the oxide layers lowered the connectivity of the lattice support, leading to facile iridium dissolution.

2. RESULTS AND DISCUSSION

Amorphous IrO_x and crystalline IrO_2 exhibit a complementary relationship in terms of catalytic activity and stability according to literature precedents[9−11] and our experimental data: compared to IrO_2, IrO_x showed *ca.* 150 mV cathodic overpotential for the OER (Figure S1), while its *S*-number (defined as the ratio between the amount of evolved oxygen and dissolved iridium, $n_{oxygen}/n_{iridium}$) was lowered by a factor of 48.8 at current densities of 10 mA·cm^{-2} (Table S1)[30] (see Figures S2−S7 and Tables S2−S4 for samples preparation and remaining characterization).

2.1. The SI-SECM Titration Sequence.

The experimental setup and redox titration sequence of SI-SECM are shown in Scheme 1. The SI-SECM experiments utilize a tip electrode (top) that enables *in operando* interrogation of the substrate electrode (bottom, where the catalytic reaction of interest occurs) through an electrochemical reaction of a redox mediator orthogonal to the catalytic reaction of interest. In this work, a gold ultramicroelectrode (UME) was used as the tip electrode, iron(III) sulfate ($Fe_2(SO_4)_3$) as the redox mediator, and iridium oxides electrodeposited on platinum UME as the substrate electrode. As shown in Scheme 1a, two size-matched (25 μm in diameter) UMEs were aligned and approached to a distance of *ca.* 2−3 μm, enabling the tip to directly detect any perturbations at the substrate (see Figure S8 for details on tip−substrate alignment and collection efficiency determination).

The titration sequence proceeded as follows: first, the surface-active species on the catalyst film were in the protonated resting state (O^{2-}-H^+) at the open circuit potential (OCP) (Scheme 1a). The chemical identity of the active species was ascertained as redox states localized on lattice oxygen atoms by hard and soft X-ray absorption analyses (*vide infra*), corroborated by a large volume of literature precedents.[12−15,17,19,31−33] Upon application of anodic potentials to the substrate electrode (anodic pulse time; t_{pulse} = 20 s), the active oxygen species were deprotonated as their electrophilic hole character increased (O^{1-} and H^+) (Scheme 1b). Deprotonated oxygens were then quantified via iron-mediated redox reaction feedback at the tip (Scheme 1c). Upon switching the substrate electrode to open circuit, the cathodic potential applied to the tip electrode reduced the iron-based redox mediator ($Fe^{3+/2+}$ E° = 0.65 V vs RHE), thereby initiating spontaneous redox reactions with surface O^{1-} (positive feedback) ($Fe^{2+} + O^{1-} \rightarrow Fe^{3+} + O^{2-}$) (Scheme 1c (i)) (see Figures S9 and S10 for further details on the redox mediator). The tip titration current relaxed to the negative feedback level as the surface-bound and electrolyte-accessible active oxygen species were fully consumed (Figure S11). The collected amperograms were then integrated over time to yield the number of titrand species per electrochemically active surface area (ECSA) (Figures S12 and S13). Repeating the quantification sequence from the OCP (0.75 V vs RHE) to the

https://doi.org/10.1021/jacs.5c16721
J. Am. Chem. Soc. 2026, 148, 957−966

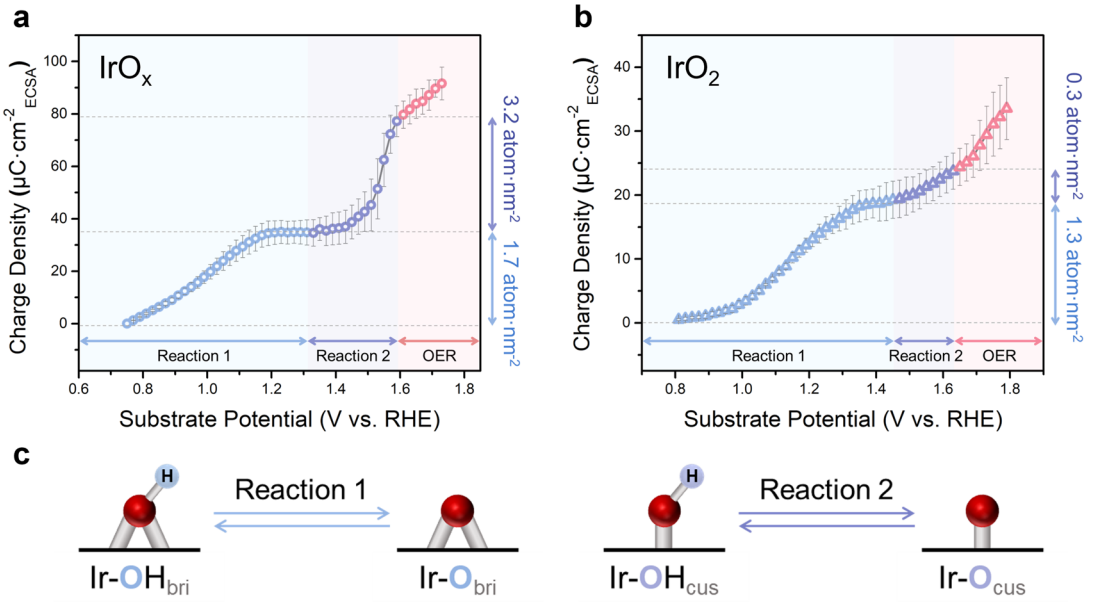

Figure 1. Redox titration curves (charge density as a function of substrate potential) for (a) amorphous IrO_x and (b) crystalline IrO_2. Active site quantification was normalized by the electrochemically active surface area (ECSA). The right *Y*-axis represents the atom density of each oxygen species (sky-blue for O_{bri} and purple for O_{cus}). (c) Schematic representation of substrate reactions within different potential ranges: the left panel illustrates reaction 1 in the sky-blue potential range, while the right panel shows reaction 2 in the purple potential range.

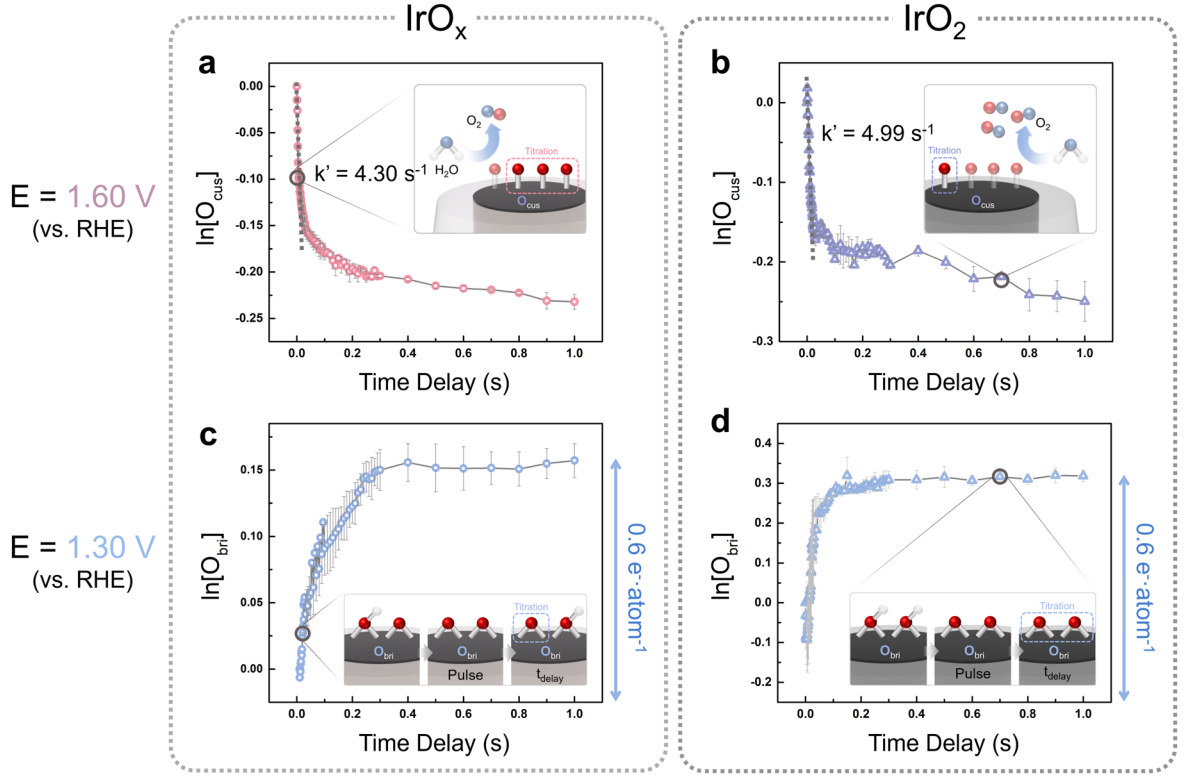

Figure 2. Time-dependent titration curves (natural logarithm of the charge density as a function of time delay) for (a, c) amorphous IrO_x and (b, d) crystalline IrO_2, indicating pseudo-first-order kinetics model (the slope of each graph) at specific reaction potentials. (a) and (b) exhibit results at 1.60 V corresponding to O_{cus} deprotonation, while (c) and (d) show results at 1.30 V where O_{bri} deprotonation occurs. The right *Y*-axis in (c) and (d) represents the charge storage capacity per O_{bri} atom.

OER (1.85 V vs RHE) resulted in the redox titration curve, reflecting the variation in surface charge density as a function of the substrate potential, E_{subs} (Figure 1).

Introducing the time delay (t_{delay}) between titrand (O^{1-}) formation and titrant (Fe^{2+}) generation yielded important kinetic parameters of the OER active species. In the absence of

https://doi.org/10.1021/jacs.5c16721
J. Am. Chem. Soc. 2026, 148, 957−966

the titrant, the titration current at the tip decays as a function of t_{delay}, due to the active site consumption via the OER (Scheme 1c (ii)) or protonation (Scheme 1c (iii)), which are chemical reactions in competition with the redox titration reaction. Time-dependent titration at specific reaction potentials yielded the rate constants for the chemical reactions by precise control of the time scales of the faster redox reaction (Figure 2). We employed an external rapid switching device that enabled the control of t_{delay} at 1 ms scale, which is a fast enough time resolution for the tracking of the reactive intermediates of OER with typical rates of several turnovers per second (Figure S14).[34]

2.2. The Redox Titration Curve of Iridium Oxides in Acidic OER. The redox titration curves provide both qualitative and quantitative insights into the electrocatalytic reactions of interest (Figure 1). A common trend was observed for IrO_x and IrO_2: both plots exhibited increases in the number of detected redox active species per unit area (ECSA) with increasing anodic substrate potential (Figure 1a,b; see also Figure S11 for the amperograms of the tip and substrate). Based on the presence of plateaus or changes in slopes, each curve was segmented into three distinct redox reaction regions color-coded in sky-blue, purple, and red, respectively. Concurrent to the findings in the literature,[12,13,17,19,31−33] we confirmed that the sky-blue potential range (0.75−1.30 V for IrO_x and 0.85−1.45 V for IrO_2) indicated oxidative deprotonation of bridging lattice oxygen (O_{bri}) (Figure 1c, reaction 1 in the left panel) and the purple potential range (1.30−1.60 V for IrO_x and 1.45−1.63 V for IrO_2) indicated oxidative deprotonation of coordinatively unsaturated site lattice oxygen (O_{cus}) (Figure 1c, reaction 2 in the right panel). The electron-deficient oxygen species designated as O_{cus} in this study includes both deprotonated water molecules absorbed on iridium coordinatively unsaturated sites and the lattice μ_1-O formed via lattice defect (see Supporting Information (page S21) for further details). The constant slope in the red region (above 1.60 V for IrO_x and 1.63 V for IrO_2) reflected the predominant occurrence of the OER.

Typically in redox titration curves, a plateau signals a surface redox equivalence.[26] A plateau in charge accumulation with increasing substrate potentials is indicative of saturation of oxidizable (such as that shown in this work) surface species. The sky-blue region for both IrO_x and IrO_2 revealed the first oxidation equivalence of the surfaces, which we designated as oxidative deprotonation of O_{bri}, and accumulation of O^{1-}, in accordance with literature precedents. The chemical identity of the lattice oxygen species is further corroborated by other experimental means such as hard and soft X-ray spectroscopies and redox kinetic isotope studies (*vide infra*). The subsequent change in slope and climb in the charge density as functions of substrate potential signaled the access of the O^{1-} species in the O_{cus} lattice sites (the purple region) for the two respective catalysts. Through the two plateaus corresponding to the two redox states, we calculated the atom densities for each active oxygen species: 1.7 ± 0.2 atom·nm^{-2} for O_{bri} and 3.2 ± 0.2 atom·nm^{-2} for O_{cus} in IrO_x (Figure 1a, right axis) and 1.3 ± 0.1 atom·nm^{-2} for O_{bri} and 0.3 ± 0.1 atom·nm^{-2} for O_{cus} in IrO_2 (Figure 1b. right axis) (see Figures S15 and S16, Tables S5 and S6, and Supporting Information (page S24) for detailed calculations and statistical analysis).

The findings collectively led to the following analysis: the calculated atom density for each oxygen species revealed that IrO_x exhibits comparable (a factor of 1.3) O_{bri} density and 10.7-fold higher O_{cus} density compared to those of IrO_2. This indicated that the structural differences are more pronounced in expression for O_{cus} than for that for O_{bri}. Moreover, O_{cus} undergoes deprotonation at more anodic potentials than that associated with O_{bri}, only slightly shy of that for OER. The significantly higher O_{cus} density in IrO_x and its proximity in the potential space to that of OER strongly suggest that O_{cus} is the OER active oxygen species.[35−37] Owing to the high reactivity of the OER active O_{cus} (see also discussions in the subsequent sections), direct spectroscopic characterization of the species has been scarce.[10,19] Our experimental findings and data analysis exhibited similar trends to that reported by Stephens and co-workers,[19] that comparable amounts of O_{cus} and O_{bri} are present in IrO_x and IrO_2 and that more active sites are expressed in IrO_x due to the structural ease of proton permeation. Quantification and discrimination in the potential space of the lattice oxygen species were feasible owing to the unique capabilities of the SI-SECM method, enabling selective probing of the electrode−electrolyte interface, which successfully overcomes the limitations of conventional surface science techniques in the investigation of complex dynamics at catalyst−solution interfaces.[21,24−29]

2.3. Time-Dependent Titrations: The OER Rate Constant Measurement. We employed time-dependent titration to investigate the reactivity of each electron-deficient oxygen species at specific reaction potentials (Figure 2). The pseudo-first-order reaction rate constants were determined by varying the t_{delay} between electron-deficient oxygen generation (O^{1-}) at the substrate and the titrant formation (Fe^{2+}) at the tip. The rate constant is determined by the slope of the graph plotting the natural logarithm of the integrated charge density (i.e., remaining O^{1-} during t_{delay}) versus t_{delay} (see Supporting Information (page S25) for details). The t_{delay} was controlled between 0 and 1 s, with intervals of 1, 5, 10, and 100 ms, using an external rapid switching device (Figure S14).[34]

As shown in Figure 2a (IrO_x) and Figure 2b (IrO_2), the amount of titrated charge decreased with increasing t_{delay} at 1.60 V, near the saturation potential of the O_{cus} in the redox titration curve (Figure 1). The decay in remaining O_{cus} indicates active sites consumption via OER during t_{delay} in the absence of other oxidizable species: oxygen can be evolved primarily via nucleophilic attack of solution H_2O.[38,39] Linear decay of the natural logarithm of the concentration of surface-active species has been typically observed for electrocatalytic reactions,[25,26] and the similar results observed here confirmed that O_{cus} is OER-active.

The observed slope of each graph represents the O_{cus} OER rate constant (k'), 4.30 ± 0.82 s^{-1} for IrO_x (Figure 2a) and 4.99 ± 0.67 s^{-1} for IrO_2 (Figure 2b; see Figures S17 and S18 and Tables S7 and S8 for statistical analysis), and indicated that an active lattice oxygen site turned over the OER four to five times per second. The similar k' values indicate that the intrinsic activity of O_{cus} is comparable across both catalyst structures at a given potential. As shown in Figure 1 and Figure S1, IrO_x reached a current density of 10 mA·cm^{-2} at 1.58 V coinciding with O_{cus} saturation, while IrO_2 exhibited a potential gap between O_{cus} charge saturation (1.63 V) and that related with 10 mA·cm^{-2} current density (1.73 V). Despite comparable O_{cus} OER activity per atom at 1.60 V, *ca.* 150 mV overpotential difference between the two catalysts is attributed to the O_{cus} density quantified by the redox titration curve (Figure 1; see the Supporting Information (page S24) for further explanation and calculations).

https://doi.org/10.1021/jacs.5c16721
J. Am. Chem. Soc. 2026, 148, 957−966

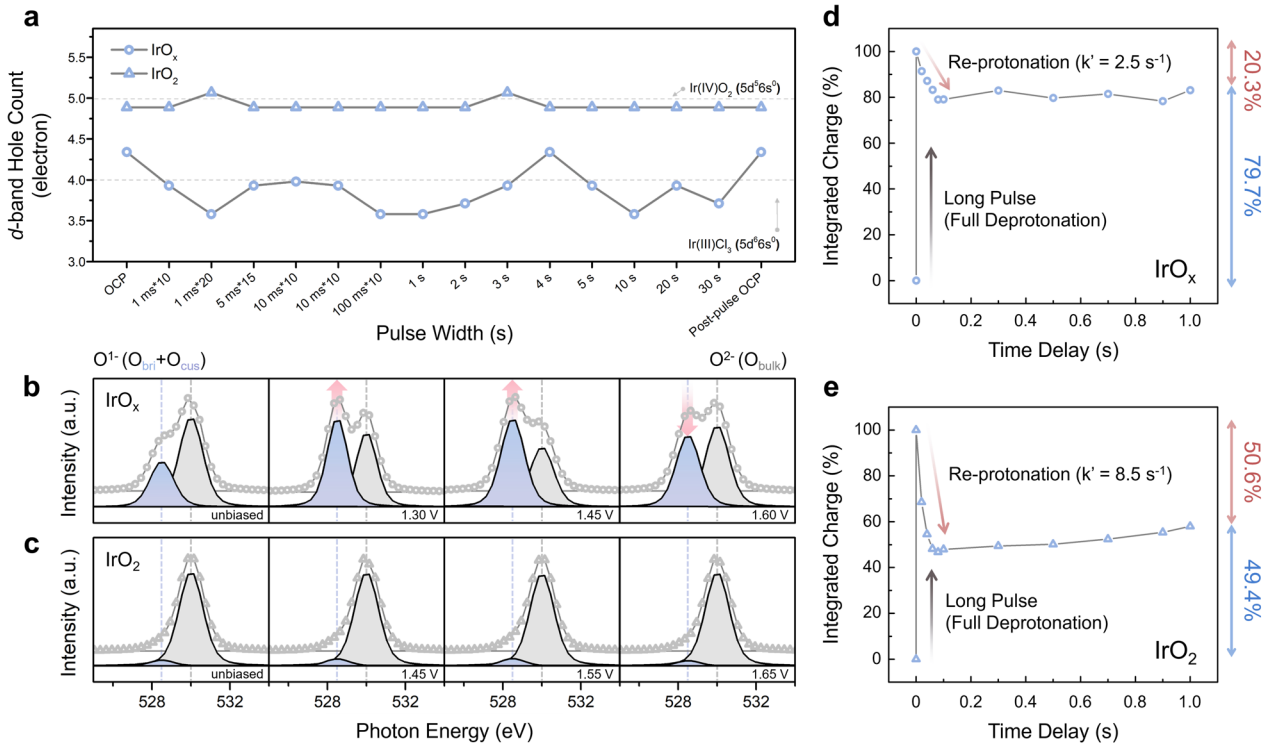

Figure 3. (a) d-band hole count variations in response to continuous pulse (IrO_x circle, IrO_2 triangle). *Operando* Ir L_3-edge spectra were recorded under the potential of reaction 1 (Figure 1c, left panel) in 0.5 M H_2SO_4. O K-edge spectra of (b) IrO_x and (c) IrO_2, measured using total electron yield (TEY) detection mode. Peak intensity variations under increasing anodic potentials are shown from left to right with the applied potential labeled in each graph. Gray-shaded peak at 530 eV denotes O^{2-} (O_{bulk}), while the sky-blue-purple colored peak at 528.5 eV corresponds to O^{1-} (O_{bri} and O_{cus}).[14,15] Note that some O^{1-} concentration was observed in the unbiased samples due to the preconditioning of the electrode to potentials where O_{bri} occurs. Time-dependent titration curves representing reprotonation kinetics following long-pulse (1.30 V) treatment for (d) IrO_x and (e) IrO_2.

An interesting anomaly (Figure 2c,d) was observed when time-dependent titration experiments were performed at 1.30 V (O_{bri} saturation potential in Figure 1): titrated charge density increased linearly with t_{delay} until reaching saturation, unlike the behavior observed at 1.60 V with O_{cus} (see Figure S19). The data signaled that O_{bri} was not consumed by OER after deprotonation (no spontaneous reaction with water); therefore, O_{bri} is not an OER-active site (see Table S9 for further explanation).[16,19,35] Typically with chemically inactive redox states in SI-SECM, no time dependence in the concentration is observed;[26] that is, the natural logarithm of the concentration remains constant at all t_{delay}, due to the preservation of the surface redox state (Figure S20). However, in the present case, we observed an increase in the redox concentration with continued anodic stimuli on the electrode. Therefore, we attributed this to the accumulation of the metastable O^{1-} lattice oxygen species (for spectral evidence refer to the subsequent section) as a function of the number of substrate potential pulse. To the best of our knowledge, this investigation is a unique explicit experimental documentation of the much-proposed charge storage mechanism in iridium oxide catalyzed acidic OER.[10,12,13,16,36,40−43] Moreover, we carried out quantitative analysis of the relationship between the stored charge and the applied potential, providing comprehensive insight into the charge storage mechanism and the implications of the stored charge on the OER kinetics and material stability (see sections below). Similar charge accumulation profiles were obtained regardless of the order of applied t_{delay} (whether starting from short t_{delay} and increasing or vice versa) (Figure S21), revealing that the charge accumulated was strictly a function of the number of applied potential pulses (also time of oxidative potential application; *vide infra*).

2.4. Analysis of the Electronic Structure of the Electron-Deficient Oxygen Species. Regarding reaction 1 centered on the O_{bri} (left panel in Figure 1c), X-ray absorption near edge structure (XANES) spectroscopy was employed to shed light on the chemical identity of the redox moiety related to the charge storage mechanism. The oxidation state of Ir was analyzed based on the white line position in the Ir L_3-edge XANES spectra. Ir(0) black ($5d^76s^2$), Ir(III)Cl_3 ($5d^66s^0$), and Ir(IV)O_2 ($5d^56s^0$), which have one electron difference in the d-band, were utilized as the reference materials (Figure S22). The Ir L_3-edge spectra of the catalyst electrodes under continuous pulses (1.35 V for IrO_x, 1.40 V for IrO_2) resulted in negligible variations in the d-band hole: IrO_x at 3.9 ± 0.3 and IrO_2 at 4.9 ± 0.1 (Figure 3a). In addition, electrodes thinned to near-nanoscale thickness, designed to increase the proportion of active-surface to core ratio, exhibited similar behavior (Table S10 and Figures S23 and S24). The apparent iridium oxidation state of 3+ in the IrO_x film results from the averaged probing, including the metallic iridium in the underlying bulk near the platinum support. Linear combination fit of the IrO_x XANES spectra (Figure S25) suggested the predominance of 4+ oxidation states in the oxide layer (see also angle-resolved XPS (AR-XPS) spectra in Tables S11 and

https://doi.org/10.1021/jacs.5c16721
J. Am. Chem. Soc. 2026, 148, 957−966

S12). More importantly, no significant oxidation state change in iridium suggested a weak link between the iridium metal centers and the time-dependent charge accumulation in Figure 2c,d. Also, for potential ranges related to reaction 2 and OER (Figure S26), little change in the oxidation state of iridium was observed for both amorphous IrO_x and crystalline IrO_2, similar to a handful of research precedents;[12−14,31,44] which led us to assume that the OER active sites are centered around electron-deficient oxygen species rather than Ir atoms. A number of literature precedents suggested that the strong overlap in the Ir 5d and O 2p orbitals allows oxidation of the lattice oxygen species to O^{1-} upon application of an anodic bias, rather than accessing higher oxidation states in iridium.[16,40,44−46] A number of research accounts reported detection of the Ir(IV) to Ir(V) transition during the water oxidation cycle;[29,31,47−50] however, presumably due to the transience of the chemical species, it was not explicitly observed in our experimental time and film thickness scales. Fitting of the AR-XPS spectra (Ir 4f; Tables S11 and S12) suggested partial involvement of the iridium(V) at the OER potentials (with more pronounced contribution at the surface—larger tilt angle), which led us to believe that Ir(V) states are involved in acidic OER; however, our experiments suggest that surface charge storage primarily occurs via the O^{1-} species (see Supporting Information (pages S33−S34) for further discussion).

The pre-edge regions of the O K-edge spectra in Figure 3b (IrO_x) and Figure 3c (IrO_2) further provided information regarding the chemical identity of the redox species in the catalytic cycle, in good alignment with the electrochemical findings from the SI-SECM data (see Figure S27 for full-range spectra). Figure 3b,c represents the O K-edge spectra of the surface states at the denoted applied potentials. In contrast to the Ir L_3-edge, changes in signal intensity were observed in response to anodic stimuli: application of 1.30 V (and 1.45 V) to IrO_x increased the intensity of the O^{1-} peak (O_{bri} + O_{cus}, sky-blue-purple peak in Figure 3b). This trend strongly suggests that the redox species responsible for charge storage in IrO_x is the electron-deficient lattice oxygens;[12,36,51] oxidizable species in the system were limited to iridium, oxygen, and solution H_2O, and we have shown (*vide supra*) that iridium and water were not oxidized at the given potential from hard X-ray absorption and SI-SECM experiments. The O K-edge spectral analysis further confirmed the chemical distinction between O_{cus} and O_{bri}. At 1.60 V the O^{1-} peak intensity decreases due to O_{cus} consumption via OER, in contrast to peak increase at 1.30 V through deprotonated O_{bri} accumulation, strongly supporting that O_{cus} is OER active and O_{bri} is OER inactive, in accordance to our SI-SECM findings (Table S9).

In the proposed charge storage mechanism (of iridium oxide acidic OER), the strong hybridization between iridium and oxygen orbitals results in positive charge sharing between the lattice cations and anions,[40,45] lowering the energy level of the oxygen p-band relative to the metal d-band: therefore, the lattice oxygens become the OER active sites via the electron-deficient states (O^{1-}).[9] First proposed by Grimaud and co-workers,[46] numerous studies have supported the mechanism;[10,12,13,36,41,42] however, experimental validation has been scarce. Our time-dependent titration clearly demonstrated the process of positive charge accumulation on the electron-deficient lattice O_{bri} (Figure 2). As the catalyst electrode was continuously exposed to anodic pulses of reaction 1 (Figure 1c), an increasing amount of O_{bri} (confirmed by the O K-edge in Figure 3b) remained deprotonated during t_{delay} (maximum 1 s), resulting in greater feedback at the tip (Figure 2c,d inset).

To further verify that charge accumulation on the surface of the elongated O_{bri} corresponds to the proton transfer in reaction 1 (Figure 1c), time-dependent titration experiments were repeated with D_2O as the proton source. As shown in Figures S28 and S29 and Tables S13 and S14, the kinetic plot revealed similar overall shape to those with H_2O at both 1.30 and 1.60 V but exhibited a normal kinetic isotope effect (KIE) value of 2.0 ± 0.5.[52,53] The slower charge accumulation in D_2O indicated that the observed oxidative transformation involves proton transfer and strongly suggests (with limited combinatory possibility invoking only iridium, water, and lattice oxygens) the deprotonation of O_{bri} (at 1.30 V). To the best of our knowledge, this is the first empirical verification and chemical identification of the charge storage process in iridium oxide catalyzed acidic OER. To rule out the catalyst detachment scenario, the effect of substrate (platinum) and dissolved O_2, identical experiments were performed on a bare Pt UME substrate and Ar-purging condition respectively: the results further confirm that the observed effects were specific to IrO_x and IrO_2 (Figures S20 and S30).

2.5. Measurement of the Lattice Oxygen Deprotonation Rate Constants and the Implications of the Protonation Equilibria on the OER Activity−Stability Trend. Numerous studies suggested the correlation between accumulated positive charge on iridium oxide surfaces and the subsequent OER catalysis.[10,16] As experimentally verified by our time-dependent titration, O_{bri} deprotonation (and slow reprotonation; *vide infra*) leads to oxidative charge accumulation.[15,16] Therefore, electrochemical investigation of the proton transfer kinetics on O_{bri} and O_{cus} is of interest, and more importantly, complete elucidation of the implications of the protonation equilibria on acidic OER catalysis is desired.

Quantitative data from Figure 2c,d reveal clear differences in the proton transfer process between the two catalysts. Dividing the saturated charge by the number of participating atoms yielded the number of redox equivalence accumulated per lattice oxygen atom: 0.6 ± 0.2 $e^-\cdot atom^{-1}$ for IrO_x, and 0.6 ± 0.1 $e^-\cdot atom^{-1}$ for IrO_2 (Figure 2c,d, right axis; see Figures S31 and S32 and Tables S15−S20 for calculation details). The per atom charge storage capacity of O_{bri} is comparable in both catalysts; however, the key difference lies in the kinetic accessibility of the deprotonated state. The IrO_x electrode (Figure 2c) required 55 anodic pulses (total time of 273 ± 30 s) to reach redox saturated surface (Table S17), whereas IrO_2 (Figure 2d) exhibited a significantly faster deprotonation rate by requiring only 27 anodic pulses (total time of 136 ± 26 s) to reach redox saturation (Table S20). To further delve into the protonation equilibria of the electron-deficient lattice oxygens, we applied long pulses matching the time required for each catalyst to reach its O_{bri} charge saturation (275 s for IrO_x and 140 s for IrO_2) and then measured the reprotonation (backward reaction in Figure 1c reaction 1) rate constants (by variation of t_{delay}; see Supporting Information (page S25) for details). As shown in Figure 3d,e, IrO_2 exhibited a much faster reprotonation rate: 2.5 ± 1.0 s^{-1} for IrO_x and 8.5 ± 0.9 s^{-1} for IrO_2 (see Table S21 for statistical analysis). This indicated that while IrO_x and IrO_2 accumulate a similar amount of charge per atom, the proton transfer rate constant (k') differed significantly: IrO_2 exhibited a much faster reprotonation rate compared to that for IrO_x.

https://doi.org/10.1021/jacs.5c16721
J. Am. Chem. Soc. 2026, 148, 957−966

Scheme 2. Representation Illustrating Structure-Dependent Penetration Depth of Electron-Deficient Oxygen Species, Governing Charge Storage Kinetics, OER Activity, and Catalyst Durability

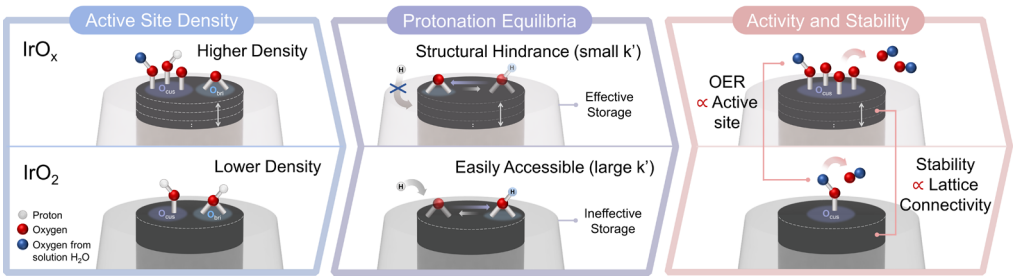

The structure dependent proton transfer kinetics can be explained by the O K-edge spectra. As shown in Figure 3b,c, the relative intensities of the O^{2-} (gray-colored peak, bulk lattice) and the O^{1-} (sky blue-purple colored peak, O_{bri} and O_{cus}) reflect the subsurface penetration of the O^{1-} species. In the case of IrO_x (Figure 3b), the intensity of O_{bri} and O_{cus} peaks varied with applied potentials, whereas no significant change (presumably due to the small population) was observed for IrO_2. This observation suggests that while O^{1-} extended to the subsurface regions of IrO_x due to electrolyte permeability, those in IrO_2 were limited to the topmost layer (Table S4 and Figure S33).[10,15,19,54] Consequently, the structure-dependent penetration depth of the elongated state of O^{1-} controlled the proton transfer kinetics and the equilibrium between the protonated and the deprotonated states. Beyond kinetic rate constants for the reprotonation of the electron-deficient lattice oxygen species, the kinematic experiments in Figure 3d,e shed light on the protonation/deprotonation equilibria. After achieving fully deprotonated O^{1-} state at 1.30 V, the system was allowed to reach equilibrium by reaction with water at OCP. At equilibrium, IrO_x retained 79.7% of its deprotonated O_{bri}, with 20.3% undergoing reprotonation, while IrO_2 retained only 49.4% of O_{bri}, with 50.6% reprotonated (Figure 3d,e). The protonation equilibrium lied heavily in favor of the deprotonated state for IrO_x, whereas that for IrO_2 favored the protonated state.

Scheme 2 summarizes the experimental findings from redox titration, electrochemical kinetics, and X-ray structural measurements in establishing the comprehensive picture of the structure-dependent active site penetration depth (lattice oxygen mediated charge storage) and its implication on the catalytic activity and stability of the materials. Amorphous IrO_x contained a higher density of active species ($O_{bri} + O_{cus}$, 4.9 ± 0.2 atom·nm^{-2}) stemming from the access of subsurface, resulting in slower deprotonation and reprotonation (k' = 2.5 ± 1.0 s^{-1}) and equilibrium favoring the oxidative charge (79.7% of O_{bri}). In contrast, crystalline IrO_2 exhibited a lower density of active species (1.6 ± 0.1 atom·nm^{-2}) confined to the catalyst surface. As a result, IrO_2 undergoes rapid deprotonation and reprotonation (k' = 8.5 ± 0.9 s^{-1}), which limited effective oxidative charge storage at equilibrium (maintaining 49.4% of O_{bri}).

Numerous studies have suggested that as oxidative charge accumulates on electron-deficient oxygen species, the activation free energy for OER decreases;[10,12,13,16,36,41,42] however, our electrochemical kinetic study revealed that the effective charge accumulation on O_{bri} does not lower the activation energy of OER at O_{cus}. From the redox titration curves in Figure 1, the OER potential ranges are comparable for the two structures (at 1.60 and 1.63 V, respectively, for IrO_x and IrO_2), despite the much larger apparent overpotential gap of *ca.* 150 mV found in conventional linear sweep voltammetry (Figure S1), which resulted from the amplification effect fueled by the 10-fold difference in the active site (O_{cus}) densities (Figure S34). Also from the slopes of Figure 2a,b, both IrO_x and IrO_2 exhibit comparable OER rate constants per atom, indicating identical intrinsic activity for OER at a given potential regardless of the crystal structure.[19] Therefore, the higher activity of IrO_x is primarily attributed to its higher O_{cus} density quantified by a redox titration curve (Figure 1, due to the subsurface propagation of O^{1-}); instead, the effective charge accumulation on O_{bri} can reduce the activation energy for O_{cus} deprotonation. Although other contributing factors, such as the surface adsorbate−adsorbate interactions,[19] need also be considered for the comprehensive understanding of the acidic OER mechanism, the difference in the active site density is a major contributor in the structure-distinct apparent reactivities in IrO_x and IrO_2 (Figure S34).

Meanwhile, the electron-deficient oxygen species also serve as key intermediates in iridium dissolution,[9,20] contributing to catalyst degradation; therefore, the active sites in IrO_x that effectively retain their oxidative deprotonation state may be more prone to dissolution. Moreover, the correlation between *S*-number (defined as the ratio between the amount of evolved oxygen and dissolved iridium, $n_{oxygen}/n_{iridium}$; see Table S1 for calculation details) measured via ICP-MS and O K-edge spectra (Figure 3) suggests that the structural robustness of the lattice supporting the active sites plays a crucial role in catalyst durability. In the case of IrO_x, most active sites are located within the electrolyte-permeable subsurface with low lattice connectivity (μ_1-O, μ_2-O; represented by the higher $O_{bri} + O_{cus}$ density), whereas IrO_2 exhibits stronger lattice connectivity (μ_3-O) directly beneath the active sites.[10] As a result, under similar O_{cus} activity, IrO_2 is more likely to retain its active sites due to robust lattice support, leading to a 151.2-fold increase in catalyst durability (Table S1). Thus, the penetration depth of electron-deficient oxygen species into the oxide layer determines proton transfer to O^{1-}, ultimately leading to the structure dependence of activity and stability of the acidic OER catalyst.

3. CONCLUSIONS

In this work, we employed the SI-SECM technique to quantify the transient reactivity of active oxygen species in amorphous IrO_x and crystalline IrO_2, correlating with structural analysis to comprehensively elucidate the factors influencing the catalytic activity and stability. The titration sequence accurately quantified significant differences from the O^{1-} penetration depth across different structures. While the intrinsic OER activity of O_{cus} (*ca.* 4.6 s^{-1}) and charge storage capacity of O_{bri}

https://doi.org/10.1021/jacs.5c16721
J. Am. Chem. Soc. 2026, 148, 957−966

(*ca.* 0.6 e^{-}·$atom^{-1}$) were comparable in both catalysts, redox titration curves revealed that IrO_x exhibits 10.7-fold higher density of the OER-active O_{cus}, compared to IrO_2. Moreover, the electrolyte permeability facilitated charge accumulation of IrO_x, exhibiting 3-fold more gradual reprotonation slope. However, efficient charge storage had a marginal effect on lowering the OER barrier itself, and the catalytic activity is primarily determined by the number of active sites. Furthermore, catalyst durability is linked to the electrolyte permeability of the material. The robust connectivity of the substrate support stabilizes the active sites, thereby enhancing the catalyst's durability. The discrete quantitative comparison using the SI-SECM technique elucidates the structure-dependent activity−stability trend, offering valuable insights for catalyst design aimed at efficient green hydrogen production. This technique and its insights can be applied to a broader range of energy conversion reactions.

■ ASSOCIATED CONTENT

Supporting Information

The Supporting Information is available free of charge at https://pubs.acs.org/doi/10.1021/jacs.5c16721.

Experimental details, materials and method, additional experimental and characterization data (LSV, CV, ICP-MS, SEM/EDS, XPS, XRD, BET, XAS), device setup, further discussions, and statistical analysis (PDF)

■ AUTHOR INFORMATION

Corresponding Authors

Sang-Il Choi − *Department of Chemistry and Green-Nano Materials Research Center, Kyungpook National University, Daegu 41566, Republic of Korea;* orcid.org/0000-0002-8280-3100; Email: sichoi@knu.ac.kr

Hangil Lee − *Department of Chemistry, Sookmyung Women's University, Seoul 04310, Republic of Korea;* orcid.org/0000-0002-0657-5660; Email: easyscan@sookmyung.ac.kr

Hyun S. Ahn − *Department of Chemistry, Yonsei University, Seoul 03722, Republic of Korea;* orcid.org/0000-0002-6014-0916; Email: ahnhs@yonsei.ac.kr

Authors

Yeonsu Kim − *Department of Chemistry, Yonsei University, Seoul 03722, Republic of Korea*

Jeonghyeon Kim − *Department of Chemistry and Green-Nano Materials Research Center, Kyungpook National University, Daegu 41566, Republic of Korea*

Complete contact information is available at: https://pubs.acs.org/10.1021/jacs.5c16721

Author Contributions

All authors have given approval to the final version of the manuscript.

Notes

The authors declare no competing financial interest.

■ ACKNOWLEDGMENTS

This work was supported by the Basic Science Research Program through National Research Foundation (NRF) of Korea (RS-2024-00337549 for H.S.A., RS-2024-00346153 for H.L. and S.-I.C., and RS-2025-02215028 for S.-I.C.), Global—Learning & Academic Research Institution for Master's·PhD students, and Postdocs (LAMP) Program of the NRF grant funded by the Ministry of Education (RS-2024-00442483), and by the Technology Innovation Program (20022479) funded by the Ministry of Trade Industry & Energy (MOTIE, Korea). This work was also supported by the NRF grant funded by the Korea government (MSIT) (RS-2025-14383258 for H.S.A., and RS-2025-21072982 for H.L.).

■ REFERENCES

(1) Nikolaidis, P.; Poullikkas, A. A comparative overview of hydrogen production processes. *Renew. Sustain. Energy Rev.* **2017**, *67*, 597−611.

(2) Carmo, M.; Fritz, D. L.; Mergel, J.; Stolten, D. A comprehensive review on PEM water electrolysis. *Int. J. Hydrogen Energy* **2013**, *38*, 4901−4934.

(3) Kibsgaard, J.; Chorkendorff, I. Considerations for the scaling-up of water splitting catalysts. *Nat. Energy* **2019**, *4*, 430−433.

(4) Chen, Z.; Duan, X.; Wei, W.; Wang, S.; Ni, B.-J. Iridium-based nanomaterials for electrochemical water splitting. *Nano Energy* **2020**, *78*, 105270.

(5) Minke, C.; Suermann, M.; Bensmann, B.; Hanke-Rauschenbach, R. Is iridium demand a potential bottleneck in the realization of large-scale PEM water electrolysis? *Int. J. Hydrogen Energy* **2021**, *46*, 23581−23590.

(6) Cherevko, S.; Zeradjanin, A. R.; Topalov, A. A.; Kulyk, N.; Katsounaros, I.; Mayrhofer, K. J. Dissolution of noble metals during oxygen evolution in acidic media. *ChemCatChem* **2014**, *6*, 2219−2223.

(7) Jovanovic, P.; Hodnik, N.; Ruiz-Zepeda, F.; Arcon, I.; Jozinovic, B.; Zorko, M.; Bele, M.; Sala, M.; Selih, V. S.; Hocevar, S.; Gaberscek, M. Electrochemical dissolution of iridium and iridium oxide particles in acidic media: transmission electron microscopy, electrochemical flow cell coupled to inductively coupled plasma mass spectrometry, and X-ray absorption spectroscopy study. *J. Am. Chem. Soc.* **2017**, *139* (36), 12837−12846.

(8) Wang, H.; Zhang, K. H. L.; Hofmann, J. P.; de la Pena O'Shea, V. A.; Oropeza, F. E. The electronic structure of transition metal oxides for oxygen evolution reaction. *J. Mater. Chem. A* **2021**, *9* (35), 19465−19488.

(9) Lončar, A.; Escalera-López, D.; Cherevko, S.; Hodnik, N. Inter-relationships between oxygen evolution and iridium dissolution mechanisms. *Angew. Chem., Int. Ed.* **2022**, *61* (14), No. e202114437.

(10) Mom, R. V.; Falling, L. J.; Kasian, O.; Algara-Siller, G.; Teschner, D.; Crabtree, R. H.; Knop-Gericke, A.; Mayrhofer, K. J.; Velasco-Vélez, J.-J. s.; Jones, T. E. Operando structure-activity-stability relationship of iridium oxides during the oxygen evolution reaction. *ACS Catal.* **2022**, *12* (9), 5174−5184.

(11) Danilovic, N.; Subbaraman, R.; Chang, K.-C.; Chang, S. H.; Kang, Y. J.; Snyder, J.; Paulikas, A. P.; Strmcnik, D.; Kim, Y.-T.; Myers, D.; et al. Activity-stability trends for the oxygen evolution reaction on monometallic oxides in acidic environments. *J. Phys. Chem. Lett.* **2014**, *5* (14), 2474−2478.

(12) Pfeifer, V.; Jones, T. E.; Velasco Vélez, J. J.; Arrigo, R.; Piccinin, S.; Hävecker, M.; Knop-Gericke, A.; Schlögl, R. In situ observation of reactive oxygen species forming on oxygen-evolving iridium surfaces. *Chem. Sci.* **2017**, *8* (3), 2143−2149.

(13) Pfeifer, V.; Jones, T. E.; Wrabetz, S.; Massue, C.; Velasco Velez, J. J.; Arrigo, R.; Scherzer, M.; Piccinin, S.; Havecker, M.; Knop-Gericke, A.; Schlogl, R. Reactive oxygen species in iridium-based OER catalysts. *Chem. Sci.* **2016**, *7* (11), 6791−6795.

(14) Pfeifer, V.; Jones, T. E.; Velasco Vélez, J. J.; Massué, C.; Arrigo, R.; Teschner, D.; Girgsdies, F.; Scherzer, M.; Greiner, M. T.; Allan, J.; et al. The electronic structure of iridium and its oxides. *Surf. Interface Anal.* **2016**, *48* (5), 261−273.

(15) Saveleva, V. A.; Wang, L.; Teschner, D.; Jones, T.; Gago, A. S.; Friedrich, K. A.; Zafeiratos, S.; Schlögl, R.; Savinova, E. R. Operando evidence for a universal oxygen evolution mechanism on thermal and electrochemical iridium oxides. *J. Phys. Chem. Lett.* **2018**, *9* (11), 3154−3160.

(16) Nong, H. N.; Falling, L. J.; Bergmann, A.; Klingenhof, M.; Tran, H. P.; Spöri, C.; Mom, R.; Timoshenko, J.; Zichittella, G.; Knop-Gericke, A.; et al. Key role of chemistry versus bias in electrocatalytic oxygen evolution. *Nature* **2020**, *587* (7834), 408−413.
(17) Kwon, S.; Stoerzinger, K. A.; Rao, R.; Qiao, L.; Goddard, W. A., III; Shao-Horn, Y. Facet-dependent oxygen evolution reaction activity of IrO2 from quantum mechanics and experiments. *J. Am. Chem. Soc.* **2024**, *146* (17), 11719−11725.
(18) BalaKrishnan, A.; Blanc, N.; Hagemann, U.; Gemagami, P.; Wonner, K.; Tschulik, K.; Li, T. Direct detection of surface species formed on iridium electrocatalysts during the oxygen evolution reaction. *Angew. Chem., Int. Ed.* **2021**, *60* (39), 21396−21403.
(19) Liang, C.; Rao, R. R.; Svane, K. L.; Hadden, J. H.; Moss, B.; Scott, S. B.; Sachs, M.; Murawski, J.; Frandsen, A. M.; Riley, D. J.; et al. Unravelling the effects of active site density and energetics on the water oxidation activity of iridium oxides. *Nat. Catal.* **2024**, *7* (7), 763−775.
(20) Kasian, O.; Grote, J. P.; Geiger, S.; Cherevko, S.; Mayrhofer, K. J. The common intermediates of oxygen evolution and dissolution reactions during water electrolysis on iridium. *Angew. Chem., Int. Ed.* **2018**, *57* (9), 2488−2491.
(21) Li, T.; Kasian, O.; Cherevko, S.; Zhang, S.; Geiger, S.; Scheu, C.; Felfer, P.; Raabe, D.; Gault, B.; Mayrhofer, K. J. J. Atomic-scale insights into surface species of electrocatalysts in three dimensions. *Nat. Catal.* **2018**, *1* (4), 300−305.
(22) Bard, A. J.; Mirkin, M. V. *Scanning Electrochemical Microscopy*, 3rd ed.; CRC Press, 2022.
(23) Amemiya, S.; Bard, A. J.; Fan, F.-R. F.; Mirkin, M. V.; Unwin, P. R. Scanning electrochemical microscopy. *Annu. Rev. Anal. Chem.* **2008**, *1* (1), 95−131.
(24) Rodríguez-López, J.; Alpuche-Avilés, M. A.; Bard, A. J. Interrogation of surfaces for the quantification of adsorbed species on electrodes: oxygen on gold and platinum in neutral media. *J. Am. Chem. Soc.* **2008**, *130* (50), 16985−16995.
(25) Ahn, H. S.; Bard, A. J. Electrochemical surface interrogation of a MoS2 hydrogen-evolving catalyst: in situ determination of the surface hydride coverage and the hydrogen evolution kinetics. *J. Phys. Chem. Lett.* **2016**, *7* (14), 2748−2752.
(26) Ahn, H. S.; Bard, A. J. Surface interrogation scanning electrochemical microscopy of Ni1-x Fe x OOH (0< x< 0.27) oxygen evolving catalyst: kinetics of the "fast" iron sites. *J. Am. Chem. Soc.* **2016**, *138* (1), 313−318.
(27) Ahn, H. S.; Bard, A. J. Surface interrogation of CoPi water oxidation catalyst by scanning electrochemical microscopy. *J. Am. Chem. Soc.* **2015**, *137* (2), 612−615.
(28) Barforoush, J. M.; Seuferling, T. E.; Jantz, D. T.; Song, K. R.; Leonard, K. C. Insights into the active electrocatalytic areas of layered double hydroxide and amorphous nickel-iron oxide oxygen evolution electrocatalysts. *ACS Appl. Energy Mater.* **2018**, *1* (4), 1415−1423.
(29) Arroyo-Currás, N. y.; Bard, A. J. Iridium oxidation as observed by surface interrogation scanning electrochemical microscopy. *J. Phys. Chem. C* **2015**, *119* (15), 8147−8154.
(30) Geiger, S.; Kasian, O.; Ledendecker, M.; Pizzutilo, E.; Mingers, A. M.; Fu, W. T.; Diaz-Morales, O.; Li, Z.; Oellers, T.; Fruchter, L.; et al. The stability number as a metric for electrocatalyst stability benchmarking. *Nat. Catal.* **2018**, *1* (7), 508−515.
(31) Bozal-Ginesta, C.; Rao, R. R.; Mesa, C. A.; Liu, X.; Hillman, S. A.; Stephens, I. E.; Durrant, J. R. Redox-state kinetics in water-oxidation IrO x electrocatalysts measured by operando spectroelectrochemistry. *ACS Catal.* **2021**, *11* (24), 15013−15025.
(32) Bozal-Ginesta, C.; Rao, R. R.; Mesa, C. A.; Wang, Y.; Zhao, Y.; Hu, G.; Antón-García, D.; Stephens, I. E.; Reisner, E.; Brudvig, G. W.; et al. Spectroelectrochemistry of water oxidation kinetics in molecular versus heterogeneous oxide iridium electrocatalysts. *J. Am. Chem. Soc.* **2022**, *144* (19), 8454−8459.
(33) Pfeifer, V.; Jones, T.; Velasco Vélez, J.; Massué, C.; Greiner, M.; Arrigo, R.; Teschner, D.; Girgsdies, F.; Scherzer, M.; Allan, J.; et al. The electronic structure of iridium oxide electrodes active in water splitting. *Phys. Chem. Chem. Phys.* **2016**, *18* (4), 2292−2296.
(34) Ahn, H. S.; Bard, A. J. Switching transient generation in surface interrogation scanning electrochemical microscopy and time-of-flight techniques. *Anal. Chem.* **2015**, *87* (24), 12276−12280.
(35) Velasco Vélez, J. J.; Bernsmeier, D.; Mom, R. V.; Zeller, P.; Shao-Horn, Y.; Roldan Cuenya, B.; Knop-Gericke, A.; Schlögl, R.; Jones, T. E. Iridium oxide coordinatively unsaturated active sites govern the electrocatalytic oxidation of water. *Adv. Energy Mater.* **2024**, *14* (19), 2303407.
(36) Velasco-Vélez, J.-J. s.; Carbonio, E. A.; Chuang, C.-H.; Hsu, C.-J.; Lee, J.-F.; Arrigo, R.; Hävecker, M.; Wang, R.; Plodinec, M.; Wang, F. R.; et al. Surface electron-hole rich species active in the electrocatalytic water oxidation. *J. Am. Chem. Soc.* **2021**, *143* (32), 12524−12534.
(37) Frevel, L. J.; Mom, R.; Velasco-Vélez, J.-J. s.; Plodinec, M.; Knop-Gericke, A.; Schlögl, R.; Jones, T. E. In situ X-ray spectroscopy of the electrochemical development of iridium nanoparticles in confined electrolyte. *J. Phys. Chem. C* **2019**, *123* (14), 9146−9152.
(38) Feng, Z.; Dai, C.; Shi, P.; Lei, X.; Guo, R.; Wang, B.; Liu, X.; You, J. Seven mechanisms of oxygen evolution reaction proposed recently: A mini review. *Chem. Eng. J.* **2024**, *485*, 149992.
(39) Chen, L.; Zhao, W.; Zhang, J.; Liu, M.; Jia, Y.; Wang, R.; Chai, M. Recent Research on Iridium-Based Electrocatalysts for Acidic Oxygen Evolution Reaction from the Origin of Reaction Mechanism. *Small* **2024**, *20* (43), 2403845.
(40) Ooka, H.; Yamaguchi, A.; Takashima, T.; Hashimoto, K.; Nakamura, R. Efficiency of oxygen evolution on iridium oxide determined from the pH dependence of charge accumulation. *J. Phys. Chem. C* **2017**, *121* (33), 17873−17881.
(41) Willinger, E.; Massué, C.; Schlögl, R.; Willinger, M. G. Identifying key structural features of IrOx water splitting catalysts. *J. Am. Chem. Soc.* **2017**, *139* (34), 12093−12101.
(42) Dickens, C. F.; Montoya, J. H.; Kulkarni, A. R.; Bajdich, M.; Nørskov, J. K. An electronic structure descriptor for oxygen reactivity at metal and metal-oxide surfaces. *Surf. Sci.* **2019**, *681*, 122−129.
(43) Hao, S.; Liu, M.; Pan, J.; Liu, X.; Tan, X.; Xu, N.; He, Y.; Lei, L.; Zhang, X. Dopants fixation of Ruthenium for boosting acidic oxygen evolution stability and activity. *Nat. Commun.* **2020**, *11* (1), 5368.
(44) Liang, C.; Katayama, Y.; Tao, Y.; Morinaga, A.; Moss, B.; Celorrio, V.; Ryan, M.; Stephens, I. E.; Durrant, J. R.; Rao, R. R. Role of electrolyte pH on water oxidation for iridium oxides. *J. Am. Chem. Soc.* **2024**, *146* (13), 8928−8938.
(45) Ooka, H.; Takashima, T.; Yamaguchi, A.; Hayashi, T.; Nakamura, R. Element strategy of oxygen evolution electrocatalysis based on in situ spectroelectrochemistry. *Chem. Commun.* **2017**, *53* (53), 7149−7161.
(46) Grimaud, A.; Hong, W. T.; Shao-Horn, Y.; Tarascon, J.-M. Anionic redox processes for electrochemical devices. *Nat. Mater.* **2016**, *15* (2), 121−126.
(47) Sanchez Casalongue, H. G.; Ng, M. L.; Kaya, S.; Friebel, D.; Ogasawara, H.; Nilsson, A. In situ observation of surface species on iridium oxide nanoparticles during the oxygen evolution reaction. *Angew. Chem., Int. Ed.* **2014**, *53* (28), 7169−7172.
(48) Mo, Y.; Stefan, I. C.; Cai, W.-B.; Dong, J.; Carey, P.; Scherson, D. A. In situ iridium LIII-edge X-ray absorption and surface enhanced Raman spectroscopy of electrodeposited iridium oxide films in aqueous electrolytes. *J. Phys. Chem. B* **2002**, *106* (14), 3681−3686.
(49) Pedersen, A. F.; Escudero-Escribano, M.; Sebok, B.; Bodin, A.; Paoli, E.; Frydendal, R.; Friebel, D.; Stephens, I. E.; Rossmeisl, J.; Chorkendorff, I.; Nilsson, A. Operando XAS study of the surface oxidation state on a monolayer IrOx on RuOx and Ru oxide based nanoparticles for oxygen evolution in acidic media. *J. Phys. Chem. B* **2018**, *122* (2), 878−887.
(50) Minguzzi, A.; Locatelli, C.; Lugaresi, O.; Achilli, E.; Cappelletti, G.; Scavini, M.; Coduri, M.; Masala, P.; Sacchi, B.; Vertova, A.; et al. Easy accommodation of different oxidation states in iridium oxide nanoparticles with different hydration degree as water oxidation electrocatalysts. *ACS Catal.* **2015**, *5* (9), 5104−5115.

https://doi.org/10.1021/jacs.5c16721
J. Am. Chem. Soc. 2026, 148, 957−966

(51) Velasco-Vélez, J.; Jones, T.; Streibel, V.; Hävecker, M.; Chuang, C.-H.; Frevel, L.; Plodinec, M.; Centeno, A.; Zurutuza, A.; Wang, R.; et al. Electrochemically active Ir NPs on graphene for OER in acidic aqueous electrolyte investigated by in situ and ex situ spectroscopies. *Surf. Sci.* **2019**, *681*, 1−8.
(52) Anslyn, E. V.; Dougherty, D. A. *Modern Physical Organic Chemistry*; University Science Books, 2006.
(53) Nishimoto, T.; Shinagawa, T.; Naito, T.; Takanabe, K. Microkinetic assessment of electrocatalytic oxygen evolution reaction over iridium oxide in unbuffered conditions. *J. Catal.* **2020**, *391*, 435−445.
(54) Kasian, O.; Geiger, S.; Li, T.; Grote, J.-P.; Schweinar, K.; Zhang, S.; Scheu, C.; Raabe, D.; Cherevko, S.; Gault, B.; Mayrhofer, K. J. J. Degradation of iridium oxides via oxygen evolution from the lattice: correlating atomic scale structure with reaction mechanisms. *Energy Environ. Sci.* **2019**, *12* (12), 3548−3555.

https://doi.org/10.1021/jacs.5c16721
J. Am. Chem. Soc. 2026, 148, 957−966